Chinese Chemical Letters 32 (2021) 1111–1116

Contents lists available at ScienceDirect

Chinese Chemical Letters

journal homepage: www.elsevier.com/locate/cclet

Communication

Sub-nanopores-containing N,O-codoped porous carbon from molecular-scale networked polymer hydrogel for solid-state supercapacitor

Meiling Wang[a,d,1], Tianyuan Zhang[c,1], Mingzhu Cui[e], Weifeng Liu[a], Xuguang Liu[a,*], Jianwei Zhao[b,*], Jiadong Zhou[d,*]

[a] Institute of New Carbon Materials, Taiyuan University of Technology, Taiyuan 030024, China
[b] College of Material and Textile Engineering, Jiaxing University, Jiaxing 314001, China
[c] Department of Chemistry, University of Washington, Seattle, Washington 98195, United States
[d] School of Materials Science and Engineering, Nanyang Technological University, Singapore 639798, Singapore
[e] Institute of Crystalline Materials, Shanxi University, Taiyuan 030006, China

ARTICLE INFO

Article history:
Received 15 July 2020
Received in revised form 4 August 2020
Accepted 17 August 2020
Available online 19 August 2020

Keywords:
Hydrogel
Sub-nanopores
Carbonization-activation
Porous carbon
Heteroatomdoping
Solid-state supercapacitor

ABSTRACT

A template-free carbonization-activation route is developed to fabricate sub-nanopore-containing porous carbon by using a novel polypyrrole (PPy) hydrogel as a precursor. This design of PPy hydrogel precursor containing molecular-scale grids (diameter ~2.0 nm) allows for homogeneous N,O-codoping into the porous carbon scaffold during the pyrolysis process. A subsequent activation step produces activated porous carbons (APCs) with tailored pore structures, which renders the APCs abundant sub-nanopores on their surface to increase the specific capacitance as extra capacitance sites. Coupled with large specific surface area and abundant heteroatoms, the optimized APC4/1 displays excellent specific capacitance of 379 F/g for liquid-state supercapacitor and 230 F/g for solid-state supercapacitor. The solid-state supercapacitor shows a high energy density of 22.99 Wh/kg at power density of 420 W/kg, which is higher than most reported porous carbon materials and satisfy the urgent requirements of elementary power source for electric vehicles. Moreover, this method can be easily modified to fabricate sub-nanopore-containing porous carbons with preferred structures and compositions for many applications.

As the leading materials in practical applications, nanoporous carbon has been commonly used in supercapacitors (SCs) [1] owing to their large specific surface area, excellent electrical conductivity and outstanding electrochemical stability [2–4]. However, nanoporous carbon-based SCs are still limited by relatively low energy density [5]. Increasing the specific capacitance of carbon materials mainly includes two routes: 1) Enhancing their electrochemical double-layer (EDL) capacitance; 2) introducingextra *pseudo*-capacitance.

The EDL capacitance of carbon-based electrodes is strongly correlated to the specific surface area (SSA) and pore structures [6,7], while introducing surface groups [8–19] will contribute to extra *pseudo*-capacitance. Notably, it is not that the larger the SSA, the higher the EDL capacitance, because the gravimetric capacitance would be saturated at ultrahigh SSA for most porous carbons as a result of a space charge capacitance originating from the space charge gradient layer on the electrode side [20]. Interestingly, it has been revealed that ions desolvation in sub-nanopores (< 1 nm) can lead to significantly enhanced EDL capacitance, and the efficiency of pore filling is optimal for EDL formation when pore size is smaller than 1 nm [21–23]. Visibly, designing of finely tuned nanoporous carbon with sub-nanopores [24] in a more cost-effective and efficient way is highly needed.

Given that the pore size distribution is predominantly determined by carbon precursors and activation process [25], rationally designing carbon precursor with desired pore structure (*e.g.*, microspore) [26], would be a clever strategy to produce sub-nanopore-containing porous carbon. Conductive polymer hydrogels with 3D networked structures recently developed by cross-linking the conjugated polymer chains using molecules with

* Corresponding authors.
E-mail addresses: liuxuguang@tyut.edu.cn (X. Liu), jwzhao@zjxu.edu.cn (J. Zhao), jzhou012@e.ntu.edu.sg (J. Zhou).
[1] These authors contributed equally to this work.

https://doi.org/10.1016/j.cclet.2020.08.026
1001-8417/

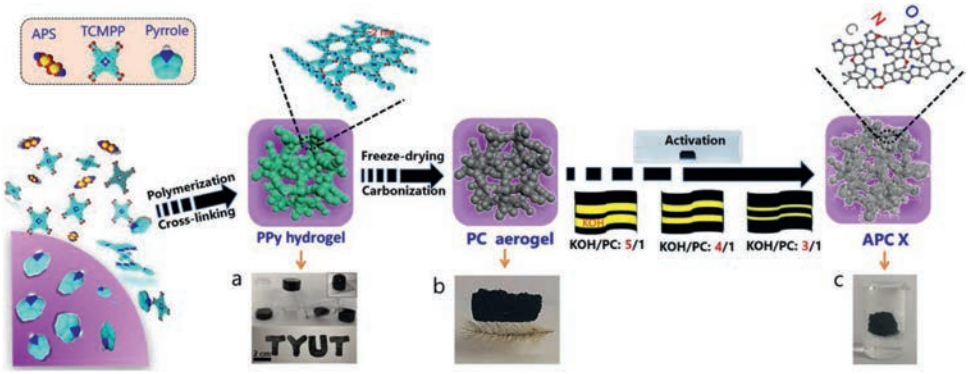

Fig. 1. Schematic illustration of the preparation processof APC from PPy hydrogel: (a) PPy hydrogel; (b) PC aerogel standing on beards of a plant; (c) APC sample floating on water.

multiple functional groups has attracted wide attention [27,28]. As is well known, the cross-linker is a key factor for preparing polymer hydrogel [4,29], because that introduction of different cross-linkers can not only tune the morphology/structure [30,31], but also screen doping heteroatom types of hydrogel. Furthermore, the morphology and heteroatom of the hydrogel precursor can be well inherited through carbonization. It can be speculated that the more the micropores especially smaller than 2 nm are designed in the hydrogel, the richer the sub-nanopores would be in carbonization-activation product. Besides, *in-situ* heteroatom doping can also bring superiorities [32–34] including uniform doping, controllable doping amount and maintained electronic structure of adjacent carbon.

In this work, we developed a template-free precarbonization-activation method to fabricate sub-nanopore-containing N,O-codoped porous carbon based on conjugated PPy hydrogel with molecular-scale grids (diameter ~2.0 nm) as the precursorand KOH as the activator (Fig. 1). This strategy relies on the formation of a supramolecularly crosslinked PPy hydrogelprecursor doped by an oxygen bridge-containing cross-linker 5,10,15,20-tetra(4-(carboxymethyloxy)phenyl)porphyrindine (TCMPP). Density functional theory (DFT) calculations show that the binding energy between TCMPP molecule and PPy chains is much higher than the lattice energy between every pair of closely packed Py units, which renders a more stable porous structure of hydrogel precursor containing a larger amount of pores (about 2 nm). A subsequent carbonization-activation step produces N,O-codoped porous carbons (APCs) with a large amount of sub-nano/marco/meso/micropores on their surface as extra *pseudo*-capacitance sites. As a result, the optimal APC demonstrates an outstanding capacitive performance including good rate capability, high specific capacitance, and remarkable energy density in solid-state supercapacitor. This work further proves that sub-nanopores are beneficial to increasing the capacitance. It also provides a strategy for preparing sub-nanopore-containing porous carbon by using polymer hydrogel of suitable molecule-scale grids as precursor for a wide range of energy-related applications.

Figs. 2A-C show typical SEM images of PPy hydrogel, PC4/1 and APC4/1, respectively. The PPy hydrogel precursor shows a continuous porous network structure with particles of 200–300 nm in size (Fig. 2A). The PC basically remains unchanged morphology, although the macropore structure shrinks slightly after pyrolysis, and wrinkles appear on the surface (Fig. 2B). After activation by KOH, nanospheres that make up APC4/1 are reduced to 80~100 nm in size (Fig. 2C) and becomes rougher in outer surface than PC. By comparing TEM images (Figs. 2D–F), it can be found that the porosity of APC4/1(Fig. 2F) increases. Different from PC (Fig. 2H), APC (Fig. 2I) is mainly composed of amorphous carbon, as will also be demonstrated by following XRD results. Obviously, finer particle size leads to larger surface area, more structural defects, in other words, more damaged crystal structure, and consequently increased content of amorphous carbon. Besides, according to Figs. 2G-I, abundant nano-pores of about 2 nm are homogenously embedded throughout the matrix of the hydrogel, PC and APC. The pore size can be further verified by specific surface area displayed in Fig. S2 (Supporting information) and Fig. 3D, where nanopores of about 2 nm dominate in the hydrogel precursor (Fig. S2), about 1.5 nm in PC and about 0.52 nm in APC. Therefore, KOH activation plays an important role in inducing nanoporosity and nanodefects in carbon materials. Density functional theory (DFT) computations show that the binding energy between TCMPP molecule and PPy chains (Fig. S3 in Supporting information) is 98.9 kJ/mol, which is much larger than the lattice energy (9.7 kJ/mol) between closely packed Py units (Fig. S4 in Supporting information). Therefore, a stable porous structure can be formed in the PPy hydrogel and large amounts of

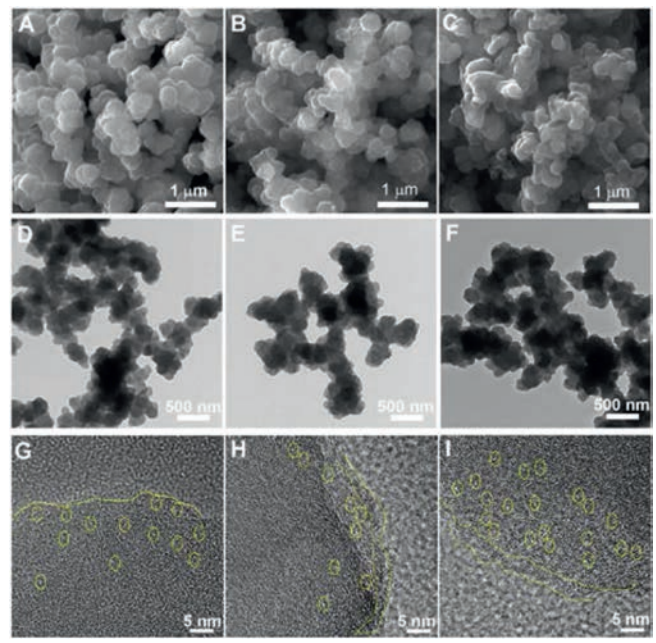

Fig. 2. SEM,TEM and HRTEM images of (A, D, G) PPy hydrogel, (B, E, H) PC4/1 and (C, F, I) APC4/1. Surrounded by yellow circles in Fig. 2G-I are some nanopores, abundant nano-pores of about 2 nm are homogenously embedded throughout the matrix of PPy hydrogel, PC and APC4/1.

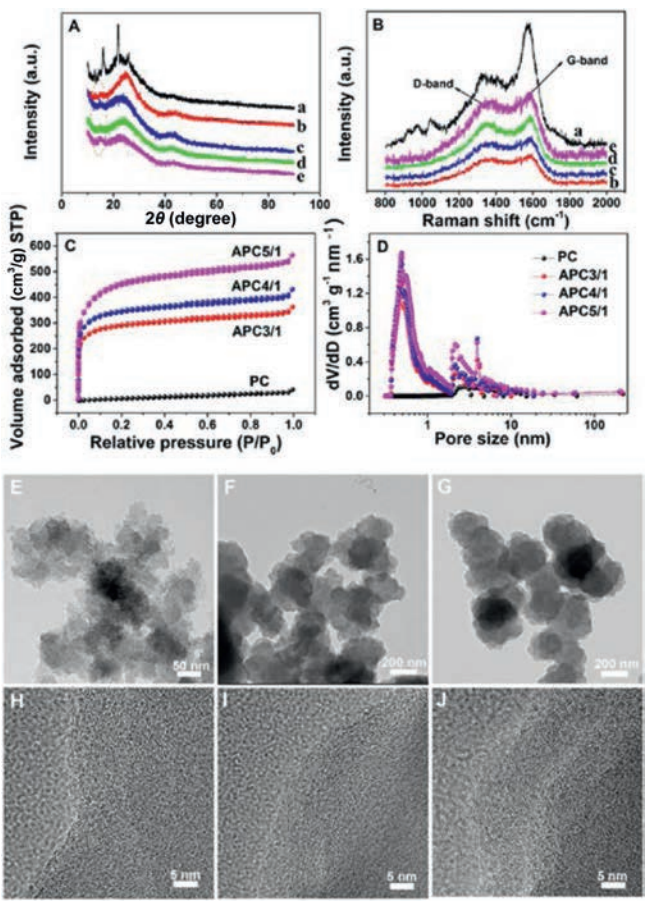

Fig. 3. (A) XRD and (B) Raman spectra of PPy hydrogel (curve a), PC4/1 (curve b), APC3/1 (curve c), APC4/1 (curve d) and APC5/1 (curve e). (C) Argon (87 K) adsorption desorption isotherm and (D) pore size distribution of PC and APCX samples by density functional theory (DFT) mode. TEM images of (E) APC3/1, (F) APC4/1 and (G) APC5/1. HRTEM images of (H) APC3/1, (I) APC4/1 and (J) APC5/1.

nanopores of about 2 nm in size makes it a good precursor to prepare sub-nanopores-containing porous carbon.

In the XRD patterns (Fig. 3A), PPy hydrogel demonstrates a broad diffraction peak at 24.1° and three sharp peaks from crosslinker. Compared with it, PC and APCX samples show three distinct diffraction peaks at $2\theta = 23.5°$, 43.5° and 79.5°, corresponding to the (002), (101) and (110) planes of a graphite phase, respectively. It should be noted that compared with those in PC, the diffraction peaks, especially the (002) peak in all APCX samples, are broadened in width and reduced in intensity, which implies increased content of amorphous carbon owing to the appearance of more damaged crystal structure [35]. And the high intensity enhancement in small-angle scattering can also be detected in all APC samples. Such phenomenon is consistent with the existence of a high content of micropores and mesopores (Table S1 in Supporting information). The development of more defects can also be demonstrated from following Raman analysis [36].

The PPy hydrogel exhibits a series of characteristic Raman bands cantered at about 931, 976, 1053, 1244, 1371, 1411 and 1588 cm^{-1} [37], which indicates the polymerization of Py in the presence of TCMPP. For both PC4/1 and APCX samples, two characteristic Raman bands at 1358 and 1598 cm^{-1} are observed, corresponding to the D (sp^3 C) and G (sp^2 C) bands, respectively. The D band can be ascribed to disordered graphite or crystal defects of carbon materials while the G band represents sp_2graphitic lattice vibration behaviour [38]. Generally, the D/G band intensity ratio is a measure of disordered graphite extent, and higher intensity ratio of D/G, suggests a more amorphous structure [39]. The ratios of I_D to I_G (I_D/I_G) of all APCX samples (0.85 for APC4/1, 0.74 for APC3/1, 0.90 for APC5/1) are larger than that of PC4/1 (0.71), implying that more ordered graphitic structure of PC is transformed into disorder carbon after activation process. In other words, activation at 700 °C brings higher amount of defect and also activates more graphitized area in PC. Higher KOH dosage results in more defects, which would bring more active sites or active surface area, thus conducive to the enhancement of capacitance [39]. In brief, Raman and XRD results indicate that activation can effectively adjust the carbon structure and the low graphitic structure of APC samples, caused by the abundant defects and pores in the sample.

Given in Figs. 3C and D are the Ar adsorption-desorption isotherms of PC and APCX samples, and their corresponding pore size distributions. The isotherms of all APCX samples show a type-I microporous structure [40]. While PC shows typical IV hysteresis (Fig. S2C), indicating a hierarchical porous structure, which confirms that KOH activation does not destroy its primary porous structure. However, the extremely slow increase trend of PC isotherm at low P/P_0 suggests it has few micropores, which again demonstratesthe regulating effect of KOH on the pore size distribution [41]. It can also be seen from the DFT pore size distribution curves (Fig. 3D) that compared with PC (Fig. S2) which show nanopores of about 1.5 nm, all APC samples show a lot of sub-nanopores of about 0.52 nm, which is consistent with size of optimized ion-accessible nanopores reported before [42–44]. With the progress of carbonization and activation, the pore size (2 nm) of the PPy hydrogel gradually decreases to ~1.5 nm (PC) and to sub-nanolevel (~0.52 nm). Therefore, the selection and activation of suitable nano-scale precursors synergistically casts the formation of sub-nanoporous carbon. According to IUPAC, the smallest pores-micropores (0.2–2 nm) [45] can be divided into super- (> 0.7 nm) and ultra-micropores (< 0.7 nm) [46]. Such ultra-micropores are more efficient for EDL formation [46]. As summarized in Table S1, the increase in KOH dosage results in an ascending trend in specific surface area and pore volume. It can be seen that micropores including sub-nanopores accounts for a high proportion in total porosity between 76.13% and 77.61%. This is due to the etching effect of KOH activator, which can proceeds as: $6KOH + C \leftrightarrow 2\,K + 3H_2 + 2\,K_2CO_3$ [47,48]. All APCX samples share similar continuous porous morphology with interconnected pore architecture, as shown in Figs. 3E-G. Close examination of the carbon backbone (Figs. 3H-J) shows that the surface roughness of all APCX samples increases as the activation level increases.

XPS spectra (Fig. 4A) show the presence of C, N and O elements in PC and all APCX samples. It has been reported that both N and O can act as electrochemically active sites to provide *pseudo*-capacitance through reversible Faraday reaction [49–51]. The elemental compositions of all APCX samples are given in Table S2 (Supporting information). On the whole, the heteroatom content, especially O element, increases with increased dosage of KOH. Although APC5/1 has highest content of heteroatoms, its N content is reduced, which is not conducive to the improvement of conductivity, so appropriate activation degree is desired to realize uniform doping of heteroatoms. APC4/1 exhibits a more suitable N and O contents of 3.0 wt% and 12.74 wt%, respectively. The deconvolution of O 1s peaks reveals the distribution of oxygen functionalities, as listed in Table S3 (Supporting information) which shows that most O in APC samples is chemically bonded to porous carbon, only a very small portion of O is physically absorbed. The N 1s spectra (Figs. 4C, G–I) suggest that all samples include pyridinic N (N-6, 397.5 eV), graphitic N (N-C, 400.6 eV) and N oxide (N-O, 402.9 eV). All these can bring various electronic environments for adjacent-atoms and further create different active sites. The deconvolution of N 1s peaks reveals the

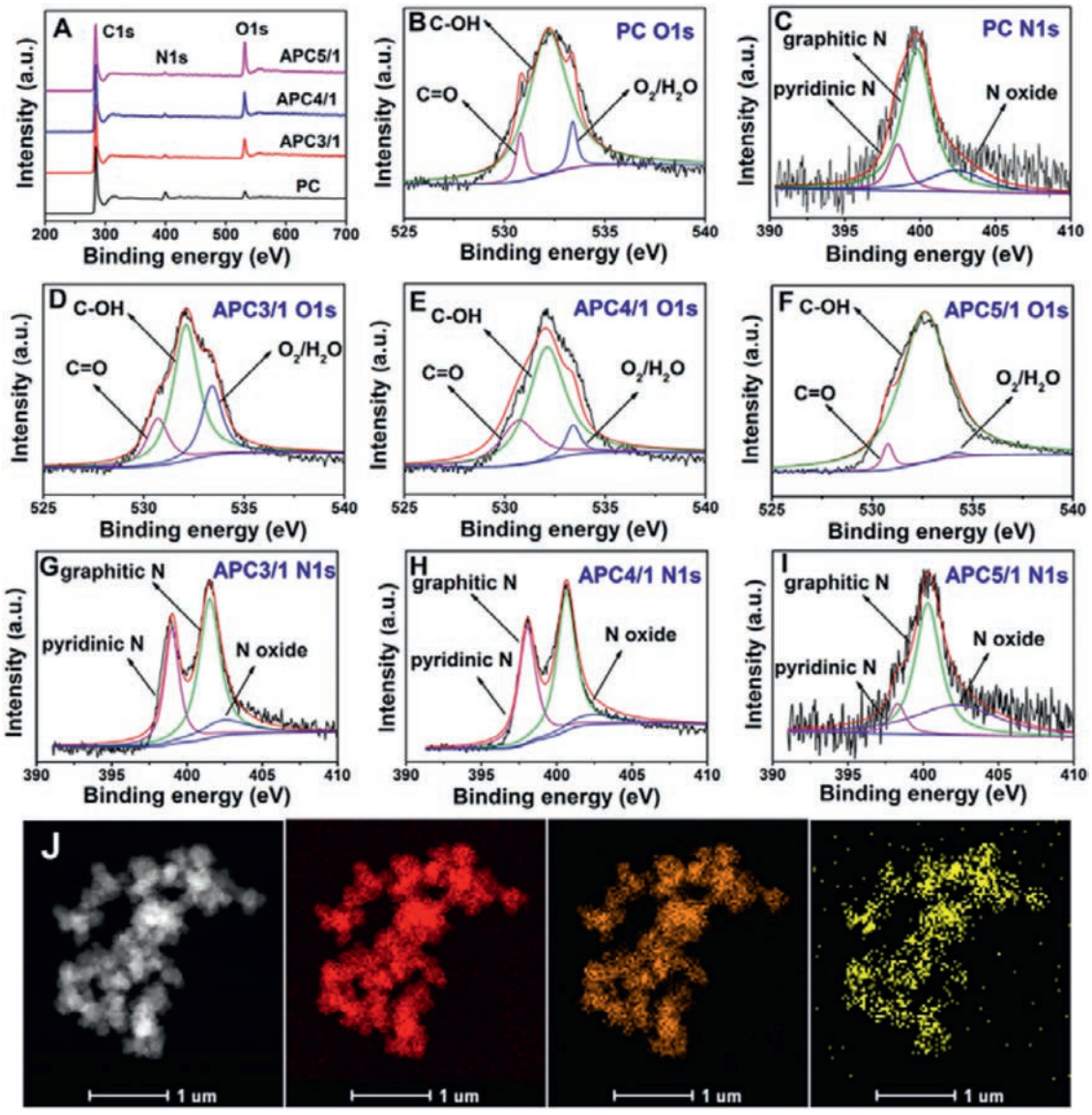

Fig. 4. XPS survey spectra for (A) PC and APC samples. Fitted high-resolution XPS spectra of (B, D-F) O 1s and (C, G-I) N 1s for PC and APC samples. (J) STEM-EDS elemental mapping images of APC4/1.

distribution of N functionalities, as shown in Table S4 (Supporting information). Abundant defects and pores are generated in APC4/1 as exhibited above, which leads to high amount of exposed N-O and edge N-6, further enhancing its electron-transform ability. In addition, both them can also improve the wettability of the carbon skeleton, so that the specific surface area accessible to electrolyte ions can be significantly increased, thereby accelerating the migration of ion. The elemental mapping of C, N and O was conducted on the basis of the STEM image of APC4/1 (Fig. 4J). The result demonstrates that all elements are uniformly distributed across the sample surface.

N,O-codoped APCs with developed porosity and skeleton are expected to be ideal electrodes for supercapacitors. Accordingly, the CV curves of all samples at a scan rate of 10 mV/s and potential range of -0.2∼0.8 V are shown in Fig. S5A (Supporting information). All CV curves exhibit near rectangular shapes, indicating an ideal double-layer capacitive behaviour for all APC samples. Note that they also show wide reversible humps, which indicate a large *pseudo*-capacitive contribution to the overall performance related to the N,O-functionalities. These wide humps evidence that proton exchange occurs when the samples are polarized during the reversible redox reaction [52] for that N, O incorporated into the carbon matrix can enhance the wettability between the electrolyte and electrode materials [53]. In addition, the pyridinic N in the carbon skeleton periphery provides electron donor properties [54]. The integral area of APC4/1 electrode is significantly larger than those of APC3/1 and APC5/1, which indicates that the capacity of APC4/1 is the largest. Even at 1000 mV/s, APC4/1 gives a CV curve same in shape as that at low scan rates in 0.5 mol/L H_2SO_4 (Fig. S5B in Supporting information). It can be seen thatat the current density of 0.5 A/g, the specific capacitance of APC3/1, APC4/1, APC5/1 electrodes is 255 F/g, 379.12 F/g and 272.87 F/g, respectively, as calculated from GCD profiles (Fig. S5C in Supporting information). Although the specific surface area of APC4/1 is smaller than that of APC5/1, it contains a higher content of N-6 and N-O, which is conducive to the improvement of electrical conductivity, and thus to the increase in specific capacitance. Besides, although the porous volume of APC5/1 is very high, an adequate pore size ration is more important for obtaining high capacitance [24]. Also it has been established that the gravimetric

capacitance of activated carbons is limited even for the most porous samples exhibiting a very high SSA [55,56]. Herein, the capacitance of APC5/1 electrodes decreases slightly though its SSA is 1642 m^2/g, this capacitance saturation can be attributed to the space charge capacitance [20]. The specific capacitance of APC4/1 electrode is also higher than those of some reported porous carbon electrodes, as shown in Table S5 (Supporting information). APC4/1 carbon shows a capacitance retention of 50% at 10 A/g, which is comparable to mesoporous grapheme [57], 3D strutted grapheme [58] and thin-film grapheme [59] electrodes. No obvious IR-drop observed, indicating an ideal reversibility of APC 4/1 electrodes (Fig. S5D in Supporting information).

In order to explore the possibility of APC as a potential supercapacitor material, symmetric liquid-state supercapacitor cells were fabricated by using two APC electrodes sandwiched with H_2SO_4-soaked separator. As shown in Fig. S5E (Supporting information), compared with three-electrode system, the working voltage of the liquid-state supercapacitor is enlarged to 1.0 V. At 10 mV/s, all devices exhibit near rectangular shapes with slight distortion, which is characteristic of electrochemical capacitor. Some weak humps are observed, especially for APC4/1-based LSC device, owing to the contribution of *pseudo*-capacitive. Among all these devices, ANPC4/1-based device has the largest CV curve area, which is consistent with the GCD results shown in Fig. S5F (Supporting information) and Fig. 5G. The CV curves of APC4/1 based device remain an unchanged shape even at a high scan rate of 300 mV/s (Fig. S5H in Supporting information), which can be attributed to its high conductivity. Obviously, the typical GCD curves with a triangular shape show an obvious distortion and small plateaus, which is also indicative of *pseudo*-capacitive behaviour due to the Faraday reaction of heteroatoms [60], along with electric double layer behaviour. In Fig. S5I (Supporting information), the GCD curves at current densities from 1 A/g to 10 A/g retain an unchanged shape at all applied current densities, suggesting that the device exhibits good capacitive characteristics. Besides, the maximum specific capacitance of 379 F/g for APC4/1 device is obtained at current density of 1 A/g and 70% of the initial value is retained at a current density up to 10 A/g. This is also related to its high conductivity as shown in Fig. S5J (Supporting information) that APC4/1-based LSC exhibits the smallest interfacial charge transfer resistance (R_{ct}) obtained from the diameter of the semicircles.

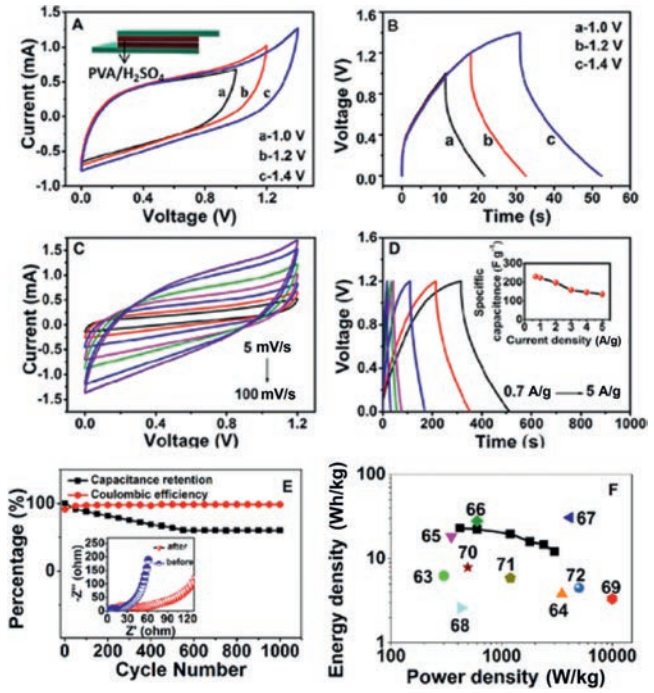

Fig. 5. (A) CV curves of APC4/1//APC4/1 all solid-state supercapacitor (SSC) recorded within different working potential windows. Scan rate: 50 mV/s. (B) GCD cycles for SSC in the voltage windows of 0-1.0 V, 0-1.2 V and 0-1.4 V at current density of 4 A/g. (C) CV curves of the solid-state device at scan rates of 5-100 mV/s. (D) GCD curves of the SSC recorded at different current densities. (E) Cycle life of the SSC at 5 mA/cm^2. (F) Ragone plots comparing the APC-SSC to recently reported PC-based SSC devices. Inset: Nyquist plots of APC4/1//APC4/1 before and after stability test.

CV curves of APC4/1//APC4/1 solid state supercapacitor measured in different potential windows are shown in Fig. 5A. Representative GCD cycle at 4 A/g tested for each voltage window is shown in Fig. 5B. Obviously, compared with LSC, this SSC shows much broader voltage window. The discharge curves are not ideally straight lines, implying a Faradic reaction process caused by N,O-codoping. A large voltage drop appears at 1.4 V, which leads to the poorest rate performance at 1.4 V. Therefore, the capacitive behaviours of the solid device are studied by CV in the range of 0–1.2 V with the scan rate ranging from 5 mV/s to 100 mV/s (Fig. 5C). The CV plots are symmetrical and deviate from a rectangular shape owing to the surface electro-sorption of H^+ and the consecutive reversible surface redox reactions of heteroatoms [61]. The absence of redox peaks implies the device is charged and discharged at a *pseudo*-constant rate during the scanning process. In the GCD curves of the solid-state device as shown in Fig. 5D, the IR drop increases with increasing testing current as a result of the large internal resistance of the device. About 60% retention of the initial specific capacitance is obtained after 1000 cycles of GCD test, highlighting the stability of SSC (Fig. 5E). Before stability test, the solid state device display a typical relatively steep line in the low frequency region of the Nyquist plots, which is caused by electric double layer effect (inset in Fig. 5E). The diffusion of H^+ from solution into the internal pore channels was also demonstrated from a conspicuous Warburg curve with a 45° slope in the intermediate frequency region [62]. The small semicircle in the high frequency region implying fast charge transfer processes. After 1000 cycles of GCD test, the electric resistance increases from 25 Ω to 55 Ω, which explains why stability is reduced. The cycle number has been increased to 10,000 cycles, however, the performance drop a lot. There are a lot of O elements on the surface, which contribute a lot of *pseudo*-capacitance, may influence its stability. The areal power and energy densities of the solid state supercapacitors at various current densities are shown in Fig. 5F. The energy densities of the device is in the range of 420−3000 W/kg at the power density of 22.99− 12.09 Wh/kg, which is much higher than that for most of heteroatom-doped carbon-based supercapacitors previously reported [63–72].

The charge/discharge time of two or three assembled devices connected in series is twice or triples that of a single device; meanwhile the voltage range retains the same (Fig. 6A). Besides, a double or threefold increase in voltage range is obtained when devices are connected in parallel (Fig. 6B). Thus, our SSCs connected in either series or parallel meet the growing demand of smart integrated electronics. Besides, for further practical demonstration, two serially-connected SSCs can continuously power a red LED bulb (2.2 V) for around 20 min (Fig. 6C). Three serially-connected SCs can continuously power four or five LED bulbs (1.8–2.2 V) for around 5 min which constitute the logo of "TYUT" (Fig. 6D).

In conclusion, we have developed a cost-effective and scalable approach to fabricate sub-nanopore-containing porous carbon (APC), simply by carbonization-activation of PPy hydrogel obtained from polymerization of pyrrole in the presence of oxygen bridge-containing cross-linker. The resultant APC shows high surface area,

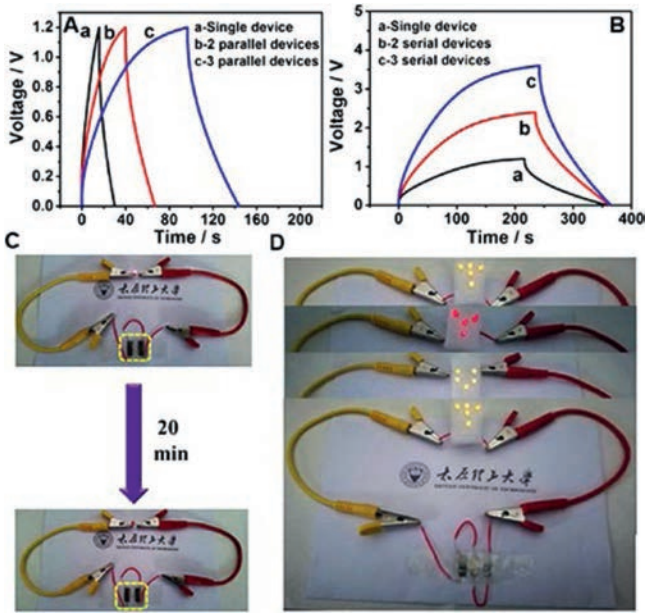

Fig. 6. (A) GCD curves of three serially-connected SSCs at 5 A/g. (B) GCD curves of three parallelly-connected SSCs at 1 A/g. (C) Digital images of a red LED bulb powered by two SSCs connected in series. (D) Digital images of three connected SSCs for powering the logo of "TYUT".

abundant sub-nano/mirco/meso/macroporosity, network interconnected structure and rich N, O-codoping. These favourable multiple synergistic characteristics endow APC with excellent specific capacitance of 379 F/g for liquid-state supercapacitor and 230 F/g for solid-state supercapacitor. Moreover, the solid-state supercapacitor shows a high energy density of 22.99 Wh/kg at a power density of 420 W/kg. This work presents a new route in rendering APC abundant sub-nanopores on its surface to increase the specific capacitance as extra *pseudo*-capacitance sites. We anticipate that this route will also be useful for developing other electrode material with desired structures and heteroatoms for a lot of applications.

Declaration of competing interest

The authors declare that they have no known competing financial interests or personal relationships that could have appeared to influence the work reported in this paper.

Acknowledgments

We gratefully acknowledge the financial support from National Natural Science Foundation of China (Nos. 51902222, 51603142, U1610255), Key Laboratory of Yarn Materials Forming and Composite Processing Technology, Zhejiang Province (No. MTC2019-03), Scientific and Technological Innovation Programs of Higher Education Institutions in Shanxi (Nos. 2019L0164 and 2019L0255), the Shanxi Provincial Key Innovative Research Team in Science and Technology (Nos. 2015013002-10 and 201605D131045-10), Key R&D Program of Shanxi Province (International Cooperation, No. 201903D421077).

Appendix A. Supplementary data

Supplementary data associated with this article can be found, in the online version, at https://doi.org/10.1016/j.cclet.2020.08.026.

References

[1] K.B. Wang, R. Bi, Z.K. Wang, Y. Chu, H. Wu, New J. Chem. 44 (2020) 3147–3167.
[2] J. Chmiola, C. Largeot, P.L. Taberna, P. Simon, Y. Gogotsi, Angew. Chem. Int. Ed. 47 (2008) 3392–3395.
[3] C. Ania, V.J.A.F.M. Khomenko, E. Raymundo-Pinero, J.B. Parra, F. Béguin, Adv. Funct. Mater. 17 (2007) 1828.
[4] Y. Shi, L. Pan, B. Liu, et al., J. Mater. Chem. A 2 (2014) 6086–6091.
[5] F. Su, C.K. Poh, J.S. Chen, et al., Science 4 (2011) 717–724.
[6] I.S. Son, Y. Oh, S.H. Yi, W.B. Im, S. Chun, Angew. Chem. Int. Ed. 159 (2020) 283–291.
[7] L. Miao, X. Qian, D. Zhu, et al., Chin. Chem. Lett. 30 (2019) 1445–1449.
[8] L.F. Chen, Z.H. Huang, H.W. Liang, H.L. Gao, S. Yu, Adv. Funct. Mater. 24 (2014) 5104–5111.
[9] Y.Q. Zhao, M. Lu, P.Y. Tao, et al., J. Power Sources 307 (2016) 391–400.
[10] D. Yan, Y. Wu, R. Kitaura, K. Awaga, J. Mater, Chem. A 7 (2019) 26829–26837.
[11] F. Yang, S. Zhang, Y. Yang, et al., Electrochim. Acta 328 (2019) 135064.
[12] G. Li, J. Sun, W. Hou, et al., Nat. Commun. 7 (2016) 1–10.
[13] Y. Liu, M. Zhang, L. Wang, et al., Chin. Chem. Lett. 31 (2020) 805–808.
[14] H. Li, J. Li, A. Thomas, Y. Liao, Adv. Funct. Mater. 29 (2019)1904785.
[15] J.T. Ren, C.Y. Wan, T.Y. Pei, X.W. Lv, Z.Y. Yuan, Appl. Catal. B: Environ. (2020) 118633.
[16] Z. Zhou, L. Miao, H. Duan, et al., Chin. Chem.Lett. 31 (2020) 1226–1230.
[17] K.A. Owusu, Z. Wang, L. Qu, et al., Chin. Chem. Lett. 31 (2020) 1620–1624.
[18] Q. Yu, J. Lv, Z. Liu, et al., Sci. Bull. 64 (2019) 1617–1624.
[19] X. Qian, L. Miao, J. Jiang, et al., Chem. Eng. J. 388 (2020) 124208.
[20] H. Ji, X. Zhao, Z. Qiao, et al., Nat.Commun. 5 (2014) 3317.
[21] J. Chmiola, G. Yushin, Y. Gogotsi, et al., Science 313 (2006) 1760–1763.
[22] E. Raymundo-Pinero, K. Kierzek, J. Machnikowski, F.J.C. Béguin, Carbon 44 (2006) 2498–2507.
[23] L. Eliad, G. Salitra, A. Soffer, D. Aurbach, Langmuir 21 (2005) 3198–3202.
[24] S. Kondrat, C.R. Pérez, V. Presser, Y. Gogotsi, A.A. Kornysheva, Energy Environ. Sci. 5 (2012) 6474–6479.
[25] H. Shao, Y.C. Wu, Z. Lin, P.L. Taberna, Chem. Soc. Rev. 49 (2020) 3005–3039.
[26] Z. Song, H. Duan, L. Miao, et al., Carbon 168 (2020) 499–507.
[27] J. Yang, X. Wang, B. Li, et al., Adv. Funct. Mater. 27 (2017) 1606497.
[28] Y. Guo, H. Lu, F. Zhao, et al., Adv. Mater. 32 (2020) 1907061.
[29] H. Wang, J. Li, N. Ding, et al., Chem. Eng. J. 386 (2020) 124021.
[30] Y. Shi, L. Pan, B. Liu, et al., J. Mater. Chem. A 2 (2014) 6086–6091.
[31] J. Yang, X. Wang, B. Li, et al., Adv. Funct. Mater. 27 (2017) 1606497.
[32] J. Du, Y. Zhang, H. Wu, S. Hou, A. Chen, Carbon 156 (2020) 523–528.
[33] D. Liu, Q. Li, S. Li, J. Hou, H.J.N. Zhao, Nanoscale 11 (2019) 4362–4368.
[34] Y. Gong, R. Chen, H. Xu, et al., Nanoscale 11 (2019) 2492–2500.
[35] W. Yu, H. Wang, S. Liu, et al., J. Mater. Chem. A 4 (2016) 5973–5983.
[36] X. Wu, L. Jiang, C. Long, Z.J.N.E. Fan, Nano Energy 13 (2015) 527–536.
[37] Y. Zhao, J. Liu, Y. Hu, et al., Adv. Mater. 25 (2013) 591–595.
[38] L.F. Chen, Y. Lu, L. Yu, X. Lou, Science 10 (2017) 1777–1783.
[39] K. Jayaramulu, D.P. Dubal, B. Nagar, et al., Adv. Mater. 30 (2018) 1705789.
[40] J.W.F. To, Z. Chen, H. Yao, et al., ACS Central Sci. 1 (2015) 68–76.
[41] M. Wahid, G. Parte, D. Phase, S. Ogale, J. Mater. Chem. A 3 (2015) 1208–1215.
[42] F.W. Richey, B. Dyatkin, Y. Gogotsi, Y. Elabd, J. Am. Chem. Soc. 135 (2013) 12818–12826.
[43] M. Salanne, B. Rotenberg, K. Naoi, et al., Nat. Energy 1 (2016) 1–10.
[44] K. Lee, Y. Yoon, Y. Cho, et al., ACS Nano 10 (2016) 6799–6807.
[45] K.S. Sing, Pure Appl. Chem. 57 (1985) 603–619.
[46] H. Shao, Y.C. Wu, Z. Lin, P.L. Taberna, P. Simon, Chem. Soc. Rev. 49 (2020) 3005–3039.
[47] Y. Zhu, S. Murali, M.D. Stoller, et al., Science 332 (2011) 1537–1541.
[48] B. Li, F. Dai, Q. Xiao, et al., Adv. Energy Mater. 6 (2016) 1600802.
[49] J.I. Clodt, V. Filiz, S. Rangou, et al., Adv. Funct. Mater. 23 (2013) 731–738.
[50] L. Bei, Y. Liu, H. Chen, Y. Mei, H. Li, J. Power Sources 341 (2017) 309–317.
[51] Y. Zhao, W. Ran, J. He, et al., ACS Appl. Mater. 7 (2015) 1132–1139.
[52] Q. Zhang, K. Han, S. Li, et al., Nanoscale 10 (2018) 2427–2437.
[53] H. Chen, Y. Xiong, T. Yu, et al., Carbon 113 (2016) 266–273.
[54] M. Koh, T.J.C. Nakajima, Carbon 38 (2013) 1947–1954.
[55] O. Barbieri, M. Hahn, A. Herzog, R.J.C. Kö Tz, Carbon 43 (2005) 1303–1310.
[56] H.J.E.A. Shi, Electrochim. Acta 41 (1996) 1633–1639.
[57] Z.S. Wu, Y. Sun, Y.Z. Tan, et al., J. Am. Chem. Soc. 134 (2012) 19532–19535.
[58] X. Wang, Y. Zhang, C. Zhi, et al., Nat. Commun. 4 (2013) 2905–2908.
[59] M.F. El-Kady, V. Strong, S. Dubin, R. Kaner, Science 335 (2012) 1326–1330.
[60] J. Cheng, F. Xie, Y. Liu, et al., J. Mater. Chem. A 3 (2015) 23955–23963.
[61] X. Wu, L. Jiang, C. Long, Z. Fan, Nano Energy 13 (2015) 527–536.
[62] Y. Huang, D. Wu, J. Jiang, et al., Nano Energy 12 (2015) 287–295.
[63] P. Ramakrishnan, S. Shanmugam, ACS Sustain. Chem. Eng. 4 (2016) 2439–2448.
[64] B. Huang, Y. Liu, Z. Xie, J. Mater. Chem. A 5 (2017) 23481–23488.
[65] H. Luo, Z. Liu, L. Chao, et al., J. Mater. Chem. A 3 (2015) 3667–3675.
[66] N. Yadav, M.K. Singh, N. Yadav, S.A. Hashmi, J. Power Sources 402 (2018) 133–146.
[67] R. Muchakayala, S.H. Song, J.W. Wang, et al., J. Ind. Eng. Chem. 59 (2018) 79–89.
[68] W.H. Li, K. Ding, H.R. Tian, et al., Adv. Funct. Mater. 27 (2017) 1702067.
[69] Y.N. Gong, D.L. Li, C.Z. Luo, Q. Fu, C.X. Pan, Green Chem. 19 (2017) 4132–4140.
[70] F. Ma, D. Ma, G. Wu, et al., Chem. Commun. 52 (2016) 6673.
[71] Y. Cheng, H. Liang, X. Xu, et al., Nano Energy 15 (2015) 66–74.
[72] Y. Xu, Z. Lin, X. Huang, et al., ACS Nano 7 (2013) 4042–4049.